OPEN ACCESS Freely available online

PLoS PATHOGENS

Structure of the Vesicular Stomatitis Virus N^0-P Complex

Cédric Leyrat[1☯], Filip Yabukarski[1☯], Nicolas Tarbouriech[1], Euripedes A. Ribeiro Jr.[1,2], Malene Ringkjøbing Jensen[2], Martin Blackledge[2], Rob W. H. Ruigrok[1], Marc Jamin[1]*

1 UMI 3265 UJF-EMBL-CNRS Unit of Virus Host Cell Interactions, Grenoble, France, **2** UMR 5075 CEA-CNRS-UJF, Institut de Biologie Structurale, Grenoble, France

Abstract

Replication of non-segmented negative-strand RNA viruses requires the continuous supply of the nucleoprotein (N) in the form of a complex with the phosphoprotein (P). Here, we present the structural characterization of a soluble, heterodimeric complex between a variant of vesicular stomatitis virus N lacking its 21 N-terminal residues ($N_{\Delta21}$) and a peptide of 60 amino acids (P_{60}) encompassing the molecular recognition element (MoRE) of P that binds RNA-free N (N^0). The complex crystallized in a decameric circular form, which was solved at 3.0 Å resolution, reveals how the MoRE folds upon binding to N and competes with RNA binding and N polymerization. Small-angle X-ray scattering experiment and NMR spectroscopy on the soluble complex confirms the binding of the MoRE and indicates that its flanking regions remain flexible in the complex. The structure of this complex also suggests a mechanism for the initiation of viral RNA synthesis.

Citation: Leyrat C, Yabukarski F, Tarbouriech N, Ribeiro EA Jr, Jensen MR, et al. (2011) Structure of the Vesicular Stomatitis Virus N^0-P Complex. PLoS Pathog 7(9): e1002248. doi:10.1371/journal.ppat.1002248

Editor: Félix A. Rey, Institut Pasteur, France

Received May 31, 2011; **Accepted** July 20, 2011; **Published** September 22, 2011

Funding: This research was supported by grants from the French ANR (ANR-07-001-01 (ANRAGE)), the FINOVI foundation and Lyonbiopôle. CL and FY were supported by MENRT fellowships from the French government. EAR was supported by postdoctoral fellowships from both the ANR and the FINOVI programs. The funders had no role in study design, data collection and analysis, decision to publish, or preparation of the manuscript.

Competing Interests: The authors have declared that no competing interests exist.

* E-mail: jamin@embl.fr

☯ These authors contributed equally to the work.

Introduction

Negative-sense RNA viruses include numerous major human pathogens such as influenza virus, rabies virus, measles virus and respiratory syncytial virus. The (−)RNA genome of these viruses is condensed by a viral nucleoprotein (N) into a helical nucleocapsid [1], that associates with the polymerase complex and serves as the template for RNA replication and transcription [2]. Replication of the genome thus requires a continuous supply of N molecules to encapsidate both the (+)RNA intermediate copies and the newly synthesized (−)RNA genomes in single-stranded forms [3]. For non-segmented (−)RNA viruses of the *Rhabdoviridae* and *Paramyxoviridae*, N is assisted by the viral phosphoprotein (P). P binds to nascent RNA-free N, forming a N^0-P complex (the superscript ^{0} denotes the absence of RNA) that prevents the polymerization of N and the non-specific encapsidation of host cell RNAs [4,5,6,7,8,9]. These processes are independent of each other [10] and, therefore, P has to fulfill two chaperone activities; blocking both RNA binding and self-assembly of N. P is a modular protein comprising a long N-terminal disordered region and two folded domains, a central oligomerization domain and a C-terminal nucleocapsid-binding domain, separated by a flexible linker [11,12]. The N^0-binding region is localized in the N-terminal disordered region [7,8,9], and it has been demonstrated that in vesicular stomatitis virus (VSV), a prototypical rhabdovirus, this region of P contains transient helical elements and may thus constitute a short molecular recognition element (MoRE) that folds upon binding to its partner [13].

In rhabdovirus nucleocapsids, every N molecule binds nine nucleotides in a positively charged cavity at the interface between its N- (N_{NTD}) and C-terminal (N_{CTD}) domains [14,15]. The N-RNA complex is stabilized by multiple salt bridges between the sugar-phosphate backbone of the RNA and basic residues of N, by contacts between neighboring N molecules involving hydrophobic side-to-side interactions, mainly between adjacent N_{CTD}, and by the exchange of N- and C-terminal sub-domains between adjacent N protomers (N_{NT}-arm, aa 1–21 and N_{CT}-loop, aa 340–375, respectively) [14,15]. Once formed, the N-RNA complex is stable and cannot be disassembled by full-length P [16]. However, on the basis of the N-RNA structure, we hypothesized that deletion of the N_{NT}-arm may sufficiently destabilize the N-RNA complex so that P or a peptide fragment of P containing the MoRE that binds N^0, could displace the RNA molecule.

In this study, we report the reconstitution of complexes between a recombinant N of VSV lacking the 21 N-terminal residues, $N_{\Delta21}$, and either full-length P dimer [11] or a peptide encompassing the N^0-binding MoRE of P [13], named here P_{60}, that comprises the first 60 amino acids of P, a two-amino acid linker and a C-terminal His_6-tag. The characterization by absorbance spectroscopy and size-exclusion chromatography (SEC) combined with static light scattering (MALLS) demonstrates that both $N_{\Delta21}{}^0$-P_{60} and $N_{\Delta21}{}^0$-P dimer complexes are free of RNA in solution, forming soluble heterodimers or heterotrimers, respectively. Therefore, P_{60} fulfills both chaperone activities of full-length P. The heterodimer $N_{\Delta21}{}^0$-P_{60} crystallized, but under the crystallization conditions, it assembled into a circular decamer of heterodimers very similar to the previously crystallized decameric N-RNA ring. The crystal structure of the decameric form of the $N_{\Delta21}{}^0$-P_{60} complex reveals the molecular mechanisms by which the N^0-binding MoRE of P attaches to N. NMR spectroscopy confirms that the MoRE of P binds to N in the $N_{\Delta21}{}^0$-P_{60} complex in solution as in the crystal structure and shows that the regions of

Author Summary

The negative sense RNA genome of the rhabdoviruses is encapsidated by the nucleoprotein, and the replication of the genome requires a continuous supply of RNA-free, monomeric nucleoprotein (N^0) to encapsidate the newly synthesized (+)RNA intermediate antigenomes and (−)RNA genomes. In this process, the viral phosphoprotein acts as a chaperone, forming a heterodimeric complex, named N^0-P, which prevents nascent N molecules from self-assembling and from binding to cellular RNAs. We reconstructed the N^0-P complex of the prototype rhabdovirus, vesicular stomatitis virus, and characterized its structure by crystal X-ray diffraction and solution experiments. Our results show how the N-terminal region of the phosphoprotein folds upon binding to the RNA-free nucleoprotein and how it prevents the non-specific encapsidation of host-cell RNA. This complex is soluble and heterodimeric, but by forcing it to polymerize into a crystal it associated into a circular decamer of heterodimers very similar to the previously crystallized decameric N-RNA ring. On the basis of our results, we propose a model that explains the role of the phosphoprotein in the encapsidation of newly synthesized RNA and in the initiation of RNA synthesis by the viral polymerase.

P flanking this MoRE remain flexible in the complex. Finally, these results suggest mechanisms for the encapsidation of newly synthesized RNA and for the initiation of RNA synthesis by the viral polymerase.

Results

Strategy for reconstituting the $N_{\Delta21}{}^0$-P and $N_{\Delta21}{}^0$-P_{60} complexes

Production of a mutant of N deleted of its 21 first N-terminal residues ($N_{\Delta21}$) in *Escherichia coli* led to the formation of inclusion bodies and of poorly soluble complexes, which could not be purified. In order to improve the solubility of the $N_{\Delta21}$ mutant, it was produced in *E. coli* in fusion with an N-terminal maltose binding protein (MBP) tag. The purified MBP-$N_{\Delta21}$ formed soluble, oligomeric N-RNA complexes, which eluted next to the exclusion volume of a Superdex S200 column (Figures S1A and S1B in Text S1). The presence of RNA was demonstrated by the absorbance ratio at 280 nm and 260 nm of 1.05 ($A_{280\ nm}/A_{260\ nm}$) (Figure S1C in Text S1). The MBP-$N_{\Delta21}$ monomer migrated as a single protein of about 100 kDa on a denaturing 4–20% gradient PAGE (Figure S1B in Text S1). Incubation of MBP-$N_{\Delta21}$ at 20°C overnight in the presence of P_{60} resulted in the displacement of the bacterial RNA from N, the dissociation of the oligomeric N-RNA complexes and the formation of an new species that eluted at 14.1 mL (Figure S2A in Text S1). The analysis by SEC-MALLS indicated a weight-averaged molecular mass of 92±2 kDa in agreement with the calculated molecular mass of the MBP-$N_{\Delta21}{}^0$-P_{60} complex (calculated mass: 88,326 Da (MBP-$N_{\Delta21}$)+8,053 Da (P_{60}) = 96,379 Da). The co-elution of MBP-$N_{\Delta21}$ and P_{60} was confirmed by denaturing 4–20% gradient PAGE (Figure S2B in Text S1). The complex contained much less RNA as shown by the absorbance spectrum ($A_{280\ nm}/A_{260\ nm}$ = 1.60) (Figure S2C in Text S1). After cleavage of the MBP tag with the TEV protease, the resulting $N_{\Delta21}{}^0$-P_{60} complex was purified by Ni^{2+} chelate affinity chromatography followed by SEC. The complex of $N_{\Delta21}$ with full-length P dimer [11] was then prepared by incubating the purified $N_{\Delta21}{}^0$-P_{60} complex overnight with the intact P dimer.

Solution properties of the $N_{\Delta21}{}^0$-P and $N_{\Delta21}{}^0$-P_{60} complexes

The molecular mass of the $N_{\Delta21}{}^0$-P dimer complex determined by SEC-MALLS was constant throughout the chromatographic peak indicating that the complex was monodisperse (M_w/M_n = 1.00±0.01), and the molecular mass of 104±4 kDa was consistent with that of a heterotrimer composed of one $N_{\Delta21}$ and an intact P dimer (calculated mass: 45,377 Da ($N_{\Delta21}$)+2×30,976 Da = 107,329 Da) (Figure 1) in accordance with the dimeric state of P in solution [11] and with a previous determination for the rabies virus N^0-P complex by native mass spectrometry [17]. The hydrodynamic radius (R_S) of 5.8±0.1 nm is about 1.5 fold larger than that for a globular particle of the same molecular mass (calculated R_S = 4.0 nm) reflecting the elongated shape of the complex and the existence of a long N-terminal disordered region (aa 1–106) [11,12].

The $N_{\Delta21}{}^0$-P_{60} complex contained no RNA (Figure 2A), and its R_S of 3.2±0.1 nm and molecular mass of 53±3 kDa indicated a globular 1:1 complex (Figure 2B), which agrees with the fact that P_{60} does not contain the dimerization domain of P [12,18]. The radius of gyration (R_g) of the $N_{\Delta21}{}^0$-P_{60} complex determined from SAXS data (2.7±0.1 nm) (Figure S3 and Table S1 in Text S1) was similar to that of a single N protomer extracted from the N-RNA complex (2.8 nm) [15], but the calculated curve of the extracted protein poorly fitted the experimental curve of $N_{\Delta21}{}^0$-P_{60}, probably because of the presence of P_{60} (Figures S4A and S4B in Text S1). *Ab initio* bead models reconstructed from SAXS data [19] (Figure 2C) could easily accommodate the structure of an isolated N protomer deleted of its N_{NT}-arm, except for the N_{CT}-loop, which is likely to adopt a different conformation in solution (Figure 2D). Although the low resolution of the model precluded the precise localization of P_{60}, the absence of an empty groove at the interface between N_{NTD} and N_{CTD} suggests that P_{60} could bind in this region. These results clearly show that P_{60} fulfils both chaperone functions of P in maintaining N^0 soluble and free of RNA, and because the size and flexibility of full-length P render the $N_{\Delta21}{}^0$-P complex unsuitable for X-ray crystallography and NMR studies, the $N_{\Delta21}{}^0$-P_{60} complex was used for further structural characterization.

Crystal structure of a decameric $N_{\Delta21}{}^0$-P_{60} complex

The $N_{\Delta21}{}^0$-P_{60} complex crystallized at low pH as a decameric circular complex. The structure was solved at a resolution of 3.0 Å by molecular replacement using the structure of an N protomer derived from the N-RNA complex [15] (Table 1). The structure of N in the $N_{\Delta21}{}^0$-P_{60} complex was almost identical to that of N in the N-RNA complex (rmsd = 0.96 Å) (Figure 3A and Figure S5 in Text S1) [15]. The complex contained no RNA, but instead, in each protomer, residues 6 to 35 of P_{60} were visible in a groove formed by residues of the hinge region of N (aa 200–300) at the junction between N_{NTD} and N_{CTD} (Figure 3B). Previous observations showed that the isolated N^0-binding region of P transiently populates α-helical conformers in the region 2–12 and 25–31 [13], and that residues 11 to 30 of P are essential for forming the N^0-P complex [7]. Upon binding to $N_{\Delta21}$, the second fluctuating helix is stabilized and extends from amino acids 17 to 31 (Figure 3B). The theoretical SAXS curve calculated from the crystal structure of one protomer of the $N_{\Delta21}{}^0$-P_{60} complex fits adequately the experimental curve of the soluble complex (Figure S4A and S4C in Text S1), and the structure is perfectly accommodated within the *ab initio* bead model (Figure S4D in Text S1) showing that the structure of the $N_{\Delta21}{}^0$-P_{60} complex in solution is the same as that in the crystal.

The structure of the $N_{\Delta21}{}^0$-P_{60} complex shows how the N^0-binding MoRE of P prevents both the interaction with RNA and

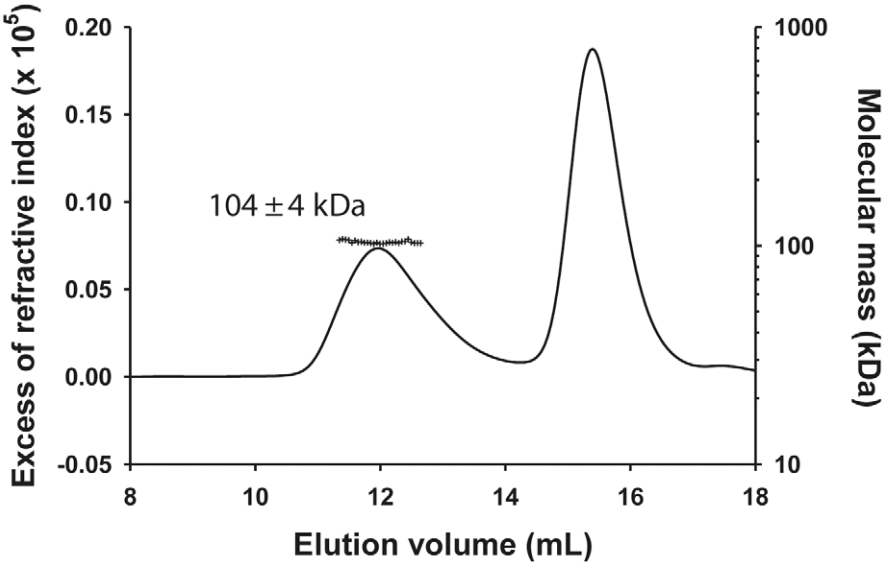

Figure 1. Heterotrimeric VSV $N_{\Delta21}{}^0$-P dimer complex in solution. The complex formed between $N_{\Delta21}$ and full-length P dimer in solution was analyzed by SEC-MALLS. The $N_{\Delta21}{}^0$-P complex elutes at 12.0 mL and the remaining $N_{\Delta21}{}^0$-P_{60} complex elutes at 15.6 mL (line). The molecular mass of 104±4 kDa (crosses) indicates a 1:2 complex between one RNA-free $N_{\Delta21}$ and two P molecules in accordance with the previous observation that P forms exclusively dimers in solution and with the N^0-P_2 complex determined for rabies virus.
doi:10.1371/journal.ppat.1002248.g001

the self-assembly of soluble RNA-free N. The binding site of P is different from that of RNA but both sites do overlap (Figures 4A, 4B and Figure S5 in Text S1), and the C-terminal turn of the α-helix of P_{60} (aa 27–31) together with the following residues (aa 32–35) block the RNA binding cavity (Figure 4A) and inhibit RNA binding. Concomitantly, the other extremity of the MoRE (aa 6–13) docks in a shallow groove on the backside of the N protomer which, in the multimeric N-RNA complex, is occupied by the N_{NT}-arm of the adjacent N_{i-1} protomer and whose bottom is made up of the N_{CT}-loop of the N_{i+1} protomer (Figure 4C and 4D). With w.t. N, the N-terminal part of the MoRE of P will compete with the N_{NT}-arm of a neighboring N molecule and therefore interferes with the polymerization of N in the absence of RNA.

The MoRE of VSV P (aa 6–35) binds to the central hinge region of N mainly through hydrophobic interactions. The amphipathic α-helix of P, together with residues 14 to 16, inserts into a hydrophobic groove of N. Tyr14 perfectly fits into a small hydrophobic pocket (Figure 5A). In addition, the complex is stabilized by three intermolecular salt bridges (Figure 5A). This region of N (aa 200–300), which also plays a central role in binding RNA is highly conserved among VSV serotypes as well as in rabies virus (RAV) [20,21] (Figure S6 in Text S1). The hinge region of VSV N exhibits 30% identity in amino acid sequence with that of RAV N, as compared with 21% and 13% for the N- and C-terminal lobes, respectively. Figure 5B shows that several hydrophobic residues lining the binding groove of P are conserved between VSV and RAV N, as well as Arg^{312}, suggesting that a similar complex forms in RAV (Figure S6 in Text S1). In the N-RNA complex, the RNA molecule interacts with N through electrostatic interactions between phosphate groups of the RNA backbone and basic residues of the protein, while the bases of three nucleotides (nt. 5, 7 and 8) are docked onto an hydrophobic surface of the RNA binding groove [15], which is also part of the MoRE binding site (Figure 5B). However, none of the basic residues of VSV N directly contacting the RNA backbone in the N-RNA complex is involved in the interaction with the MoRE of P. A similar mode of RNA binding was observed in the RAV N-RNA complex [14], but only two arginines out of the six residues involved in direct interactions with phosphate groups in the VSV complex are conserved in the RAV complex [20].

The RNA binding groove of N is rich in basic residues forming a highly positive surface area (Figure 5C), while the backside of N_{CTD} harbors a negative surface potential (Figure 5C). The MoRE of P (aa 6–35) has a bipolar distribution of charges with a positive pole at its N-terminus and a negative pole its C-terminus. In the $N_{\Delta21}{}^0$-P_{60} complex, the negative pole of P localizes in the RNA binding groove, while the positive pole docks on the backside of N_{CTD}, modifying the distribution of electrostatic potentials on these surfaces of N and suggesting that electrostatics could play a role in orientating P before binding (Figures 5C and 5D). The crystallization is at pH 4.6 and it is likely that protonation of acidic groups reduces repulsion forces that keep the $N_{\Delta21}{}^0$-P_{60} complex in its isolated form at pH 7.0.

NMR spectroscopy

In the crystal structure of the $N_{\Delta21}{}^0$-P_{60} complex residues 6 to 13 and 32 to 35 of P_{60} exhibit conformational heterogeneity (Figure S7 in Text S1), while residues 1 to 5 and 36 to 68 are not visible. To further characterize the conformational dynamics of these parts of P_{60} in the soluble $N_{\Delta21}{}^0$-P_{60} complex, we used nuclear magnetic resonance (NMR) spectroscopy. Initially, spectra of ^{15}N, ^{13}C, ^{2}H-labeled P_{60} in complex with unlabeled $N_{\Delta21}$ were recorded. In a complex of this size (53 kDa) NMR signals are significantly broadened, precluding their detection, but in the HSQC spectrum of the $N_{\Delta21}{}^0$-P_{60} complex, resonances corresponding to the last 28 amino acids of P_{60} (aa 41–60+linker+His_6 tag) are clearly visible (Figure 6A), suggesting that this tail remains free and flexible in the complex. Comparison with the free peptide showed that most resonances superimpose. Small chemical shift differences were observed for residues Q^{41} to G^{44}, probably due to the proximity of the bulk complex, and for two aromatic residues (Y^{53}, F^{54}) suggesting weak interactions of these residues with N. The amide backbone ^{15}N transverse relaxation rate constant (R_2) is

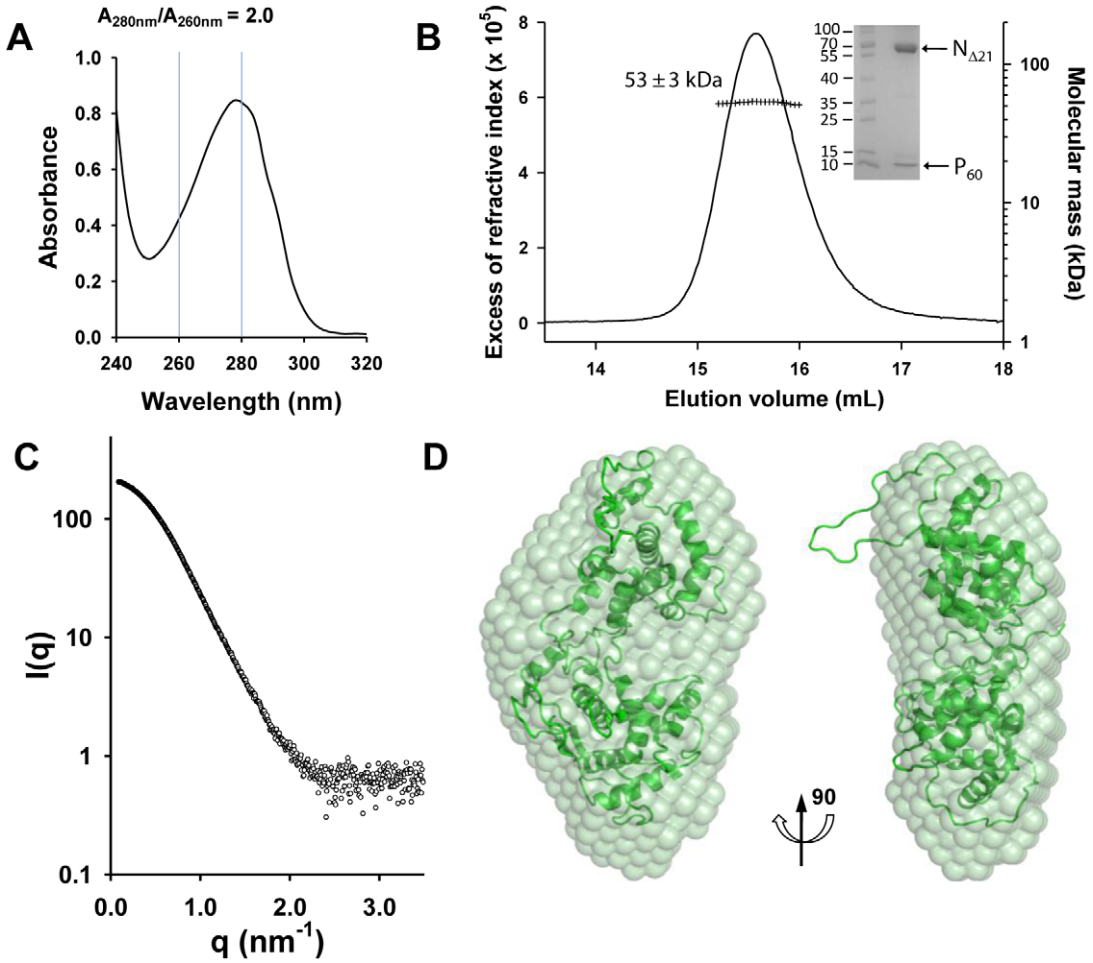

Figure 2. Heterodimeric VSV $N_{\Delta21}{}^0$-P_{60} complex in solution. (A) The absence of RNA in the complex is revealed by the UV absorbance spectrum, which exhibits an $A_{280\ nm}/A_{260\ nm}$ ratio of 2.0. (B) Analysis of the $N_{\Delta21}{}^0$-P_{60} complex by SEC-MALLS. The complex elutes as a single peak at 15.6 mL (line), and the presence of the two proteins in the complex is demonstrated by SDS-PAGE analysis of the peak fraction using Coomassie blue staining (inset). The molecular mass of 53±2 kDa (crosses) indicates a 1:1 complex between $N_{\Delta21}$ and P_{60} (calculated molecular mass = 45,377 Da ($N_{\Delta21}$)+8,053 Da (P_{60}) = 53,430 Da). (C) Experimental SAXS data (open circles) up to 3.5 nm^{-1}. The SAXS curve recorded at ESRF beamline ID 14-3 shows the scattering intensity I(q) as a function of the scattering vector, $q = (4\pi \sin\theta/\lambda)$. (D) Average *ab initio* bead model of the $N_{\Delta21}{}^0$-P_{60} complex. The N protomer extracted from the circular N-RNA complex (2GIC chain E) fits to the SAXS-derived model, except for the N_{CT}-loop.
doi:10.1371/journal.ppat.1002248.g002

sensitive to rapid fluctuations at the pico- to nanosecond time scale, as well as to chemical shift exchange on the micro- to millisecond time scale. Transverse relaxation of the visible resonances increased from the C-terminus to the region containing the bound helix, indicating a corresponding increase in rigidity of the backbone (Figure 6B). Very weak additional peaks up-field shifted in the amide proton dimension were detected in a ^{15}N-^{1}H TROSY spectrum further supporting folding of the helical element upon binding (data not shown).

In a second experiment, addition of sub-stoichiometric amounts of unlabeled $N_{\Delta21}$ attached to MBP (to maintain solubility) to ^{15}N-labeled P_{60} resulted in an overall reduction in the intensity of the peaks in the HSQC spectrum, in proportion of the amount of added MBP-$N_{\Delta21}$ indicating that a fraction of P_{60} formed a complex with MBP-$N_{\Delta21}$. Spin relaxation measurements of equilibrium mixtures of free and bound peptide refine our understanding of the dynamics of the system. Systematically larger R_2 values observed for residues 1 to 17 reveal additional contributions from chemical shift exchange (R_{ex}) that are not present in the free form of the peptide and that increase significantly upon increasing the molar ratio of MBP-$N_{\Delta21}$ to P_{60} (Figure 5C). This indicates that the N-terminal part of P_{60} experiences conformational exchange when in complex with $N_{\Delta21}$ with an interconversion rate on the micro to millisecond timescale. In the crystal structure, residues 6 to 13 bind in place of the N_{NT}-arm of the protomer N_{i-1} and pack onto the N_{CT}-loop of protomer N_{i+1} (Figures 4C and 4D), but in the isolated form of the complex, the N_{CT}-loop binding surface for these residues is missing. These results confirmed that in the solution, like in the crystal, residues 17 to 35 of P form a stable complex with N, while the flanking N- and C-terminal regions remain dynamic. The flanking C-terminal part (aa 40–60) behaves as a flexible tail and shows little evidence of interaction with N. The flanking N-terminal region (aa 1–16) interacts with N but undergoes conformational exchange. These flexible regions seem dispensable for the chaperone activities of P since a shorter peptide encompassing residues 7 to 40 of P is also capable of displacing bacterial RNA from $N_{\Delta21}$ and of forming a soluble heterodimeric 1:1 complex with this protein (data not shown).

Table 1. Data collection and refinement statistics (molecular replacement).

	Crystal 1
Data collection	
Space group	$P2_12_12$
Cell dimensions	
a, *b*, *c* (Å)	74.56, 171.97, 239.86
α, β, γ (°)	90.0, 90.0, 90.0
Resolution (Å)[a]	59.97-3.03 (3.20-3.03)
R_{sym}[a]	11.4%(28.1%)
$I/\sigma I$[a]	9(3.5)
Completeness (%)[a]	89.9 (80.7)
Redundancy	3.1 (2.5)
Refinement	
Resolution (Å)	59.97-3.03 (3.11-3.03)
No. reflections	168,372
R_{work}/R_{free}	24.4%/27.7%
No. atoms	
Protein	17,105
Water	455
R.m.s. deviations	
Bond lengths (Å)	0.006
Bond angles (°)	0.893
Ramachandran favored	92.6%
Ramachandran allowed	98.4%

[a]Values in parentheses are for highest-resolution shell.
doi:10.1371/journal.ppat.1002248.t001

Discussion

In the current study, we have determined the structure of the N^0-binding MoRE of P bound to N and demonstrated that the regions of P flanking the MoRE conserve some flexibility in the N^0-P complex. Because the N^0-P complex is required for the replication of the virus [5,22], inhibition of its formation might represent an interesting target for blocking viral replication and could explain the recent observations that a homologous peptide (P_{60}) from rabies virus P inhibits viral replication [23].

The $N_{\Delta21}{}^0$-P_{60} complex as a model of the N^0-P complex

Our results demonstrate that the reconstituted $N_{\Delta21}{}^0$-P_{60} complex is a suitable model for the viral N^0-P complex in agreement with previous studies. Both the crystal structure and the NMR spectroscopy experiments show that the MoRE of P, which adopts a stable conformation upon binding to N, includes residues 6 to 35 and corresponds closely to the fragment that was previously identified as essential and sufficient for maintaining N in a soluble form (aa 11–30) [7].

Previous studies revealed that VSV P is a dimeric and modular protein in which the N-terminal part (aa 1–106) is globally disordered [11,12,13,18,24,25]. The dimerization domain of P is localized in the central region of the protein (aa 107–177) [18] and is therefore not present in P_{60}, which is monomeric [13]. The stoichiometry of the $N_{\Delta21}{}^0$-P_{60} complex (1:1) shows that one MoRE of P is capable of binding one N molecule. The stoichiometry of the complex formed between $N_{\Delta21}$ and full-length P (1:2) in the concentration range used here suggests that a single $N_{\Delta21}$ is bound to P dimer. The remaining part of the P dimer is tethered to $N_{\Delta21}$ through a flexible linker, in agreement with the large hydrodynamic radius measured here for the $N_{\Delta21}{}^0$-P dimer complex. In isolation, the N-terminal region of P contains two transient α helices (aa 2–12 and 25–38) [13]. In the crystal structure, the second helix is stabilized and extends from residue 17 to residue 35, whereas the first helix is not present. Residues 1 to 5 are not visible and residues 6 to 13 adopt different conformations in the different protomers of the circular complex. Because NMR spectroscopy reveals that this N-terminal region of P (aa 1–17) is in chemical shift exchange, it is possible that in solution it adopts different conformations bound in different orientations on the surface of N, but that only those docked into the backside groove of N allow the packing of the $N_{\Delta21}{}^0$-P_{60} complex into crystals and were thus selected during the crystallization process.

The truncated form of N ($N_{\Delta21}$) conserves the ability of self-association in the presence of RNA and, like w.t. N, forms oligomeric N-RNA complexes when expressed in bacteria. As assumed from the structure of the oligomeric N-RNA complex [15], the N_{NT}-arm stabilizes the multimeric N-RNA complexes by linking together adjacent N protomers. The N-RNA complex formed with w.t. N could not be dissociated by the addition of full-length P or of a fragment of P encompassing the N^0-binding region. However, the deletion of the N-terminal sub-domain destabilized the complex and allowed P_{60} to displace the RNA molecule and disassemble the multimeric N-RNA complex. In a previous study, the co-expression of P with a similar variant of VSV N lacking the first 22 amino acids ($N_{\Delta22}$) led to the production of complexes of different sizes containing $N_{\Delta22}$ and P but not of N-RNA complexes, suggesting a role for the N-terminal region of N in the encapsidation of the RNA [10]. Assuming an equilibrium between the N^0-P complex and the multimeric N-RNA complex, with w.t. N, the stabilization brought by the N_{NT}-arm to the multimeric assembly would displace the equilibrium towards the formation of the N-RNA complex. In the absence of the N_{NT}-arm, the truncated N molecules assemble onto cellular RNAs as seen in our expression system, but in the presence of co-expressed P, like upon addition of P_{60} to our purified MBP-$N_{\Delta21}$-RNA complexes, the equilibrium is displaced towards the formation of the N^0-P complexes. The absence of N-RNA complex in cells co-expressing $N_{\Delta22}$ and P may not result from a default of encapsidation but rather from the displacement of the equilibrium towards N^0-P.

Unexpectedly, the $N_{\Delta21}{}^0$-P_{60} complex failed to crystallize as a heterodimer but crystallized into circular decamers of heterodimers. With the exception of the missing N_{NT}-arm, the structure of $N_{\Delta21}$ in the $N_{\Delta21}{}^0$-P_{60} complex is very similar to that of N in the decameric N-RNA complex, with less than 1 Å r.m.s.d. between the two structures. Different explanations why multimerization occurs under crystallization conditions can be proposed. Firstly, the $N_{\Delta21}{}^0$-P_{60} complex crystallized at pH 4.6 like VSV circular N-RNA complexes [15], while solution SEC-MALLS and SAXS experiments were performed at pH 7.5 and NMR experiments at pH 6.0. A modification of the electrostatic surface potential (Figures 5C and 5D) could affect the equilibrium between heterodimeric and multimeric $N_{\Delta21}{}^0$-P_{60} complex. No evidence of multimerization was, however, found in solution at pH 4.6 in the concentration range used for SEC-MALLS and SAXS experiments. Secondly, the ring-like structure of ten protomers appears as a favored organization of VSV N, likely reflecting on some geometrical and/or surface properties of the protein. VSV N forms ring-like structures mostly containing ten N subunits in the presence of non-specific RNA when expressed in a recombinant

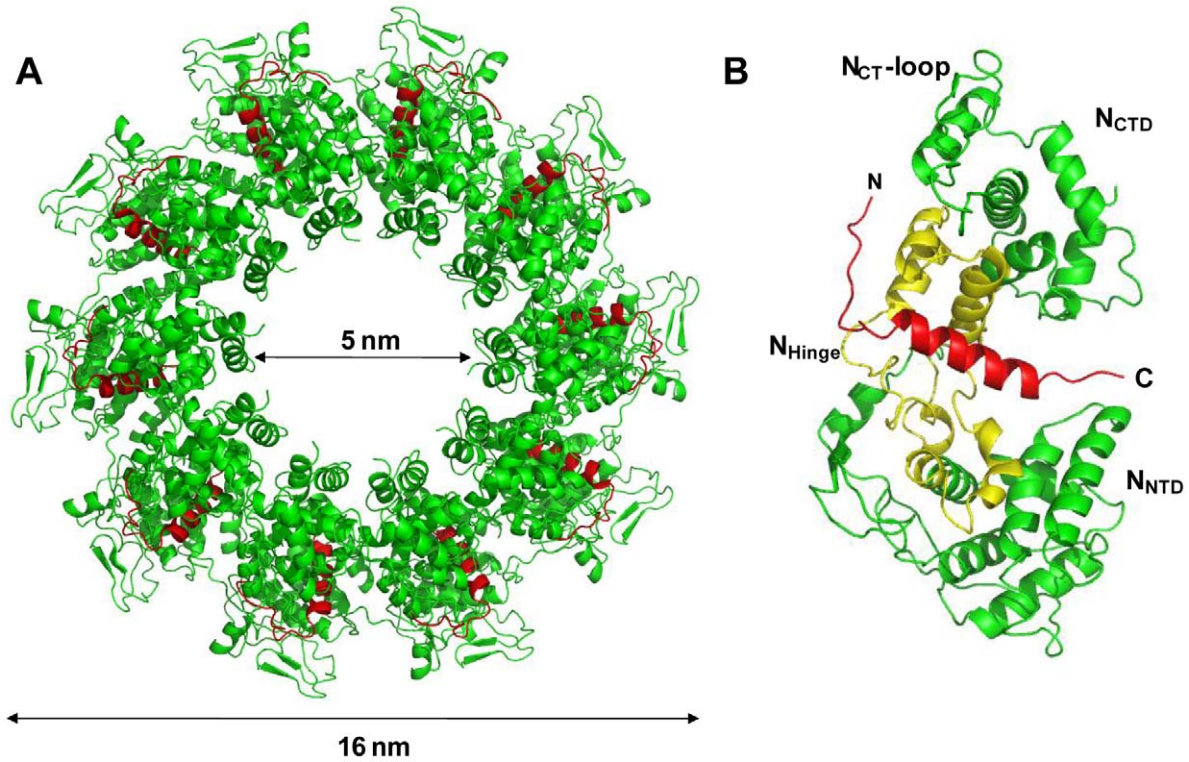

Figure 3. Crystal structure of a decameric form of the $N_{\Delta 21}{}^0$-P_{60} complex. (A) Overall structure of the decamer of $N_{\Delta 21}{}^0$-P_{60} complex. $N_{\Delta 21}$ is shown in green and P_{60} in red. (B) Ribbon representation of one protomer of $N_{\Delta 21}{}^0$-P_{60}. The central hinge region of N (aa 200–300) is shown in yellow and P_{60} (aa 6–35) is shown in red.
doi:10.1371/journal.ppat.1002248.g003

system [15,26]. The RNA can be removed from these ring-like structures without disrupting the multimeric assembly [27]. A single amino acid variant of VSV N that is no longer capable of binding RNA also crystallized into a decameric assembly of empty N molecules [10]. These circular N-RNA complexes are artifacts of the crystallization process because the actual nucleocapsid is very long and cannot form rings. However, in the virion, the nucleocapsid adopts a bullet-shaped structure composed of a trunk in which the nucleocapsid regularly spirals into superposed turns of 37.5 subunits of N and of a tip which is formed of seven turns containing varying numbers of subunits [1]. The upper turn of the bullet tip, which may represent the nucleation centre from which the particle assembles, resembles a decameric ring, suggesting that the assembly in ten members ring or spiral corresponds to an optimal side-by-side orientation between adjacent N subunits. The RNA-free $N_{\Delta 21}{}^0$-P_{60} complex is capable of assembling into circular multimers, and it seems likely that an increase of the concentration of the $N_{\Delta 21}{}^0$-P_{60} complex under the crystallization conditions together with a change in pH shift the equilibrium towards the multimers.

This raises the question of the effect of crystallization on the structure of the $N_{\Delta 21}{}^0$-P_{60} complex. The SAXS curve calculated for $N_{\Delta 21}{}^0$-P_{60} protomer extracted from the crystal structure perfectly reproduced the experimental curve of the soluble complex, while NMR spectroscopy clearly shows that the same segment of P (aa 17–35) is involved in a stable complex with N in solution and in the crystal, arguing that crystallization has no major effect on the structure of the more rigid part of the complex. In solution, the N-terminal part of the MoRE of P (aa 1–16) appears to be in conformational exchange and could thus exist in different conformers including those observed in the crystal in which residues 6 to 16 are docked onto the backside groove of N. Crystallization of the $N_{\Delta 21}{}^0$-P_{60} complex may thus select the more compact conformers and therefore not reproduce the conformational diversity of this region that is found in solution. In addition, the high conservation rate of residues of N forming the binding surface for the MoRE of P, both within VSV serotypes and between the evolutionarily more distant VSV and RAV, supports the localization of the interface between the two proteins and hints at the formation of a similar complex in RAV.

Mechanisms of chaperone activities

The characterizations in solution indicate that the $N_{\Delta 21}{}^0$-P_{60} complex is RNA-free heterodimer and that, therefore, P_{60} or a shorter fragment of P (aa 7–40) fulfill both chaperone activities of P. The crystal structure of the $N_{\Delta 21}{}^0$-P_{60} complex clearly shows how the N^0-binding region of P inhibits RNA binding by filling the RNA-binding groove of N. In solution, this part of P also forms a stable complex with N as seen by NMR spectroscopy. The structure also suggests how P prevents the self-assembly of N in the absence of RNA. In the bound form observed in the crystal structure, the N-terminal extremity of the MoRE (aa 6–16) directly competes with the N_{NT} arm of a neighboring N molecule. Assuming this region of P fluctuates between bound and free forms in the soluble N^0-P complex, the free form may act as an entropic bristle, thereby also preventing the oligomerization of N. With full-length P dimer, the flexibility and the bulkiness of the remainder of the protein may also contribute to this effect by masking the binding interfaces for RNAs or other N molecules. In addition, the MoRE of P exhibits a bipolar distribution of charges, with a positive pole at its N-terminal extremity and a negative pole at its C-terminal extremity. Binding of the MoRE of P modifies the

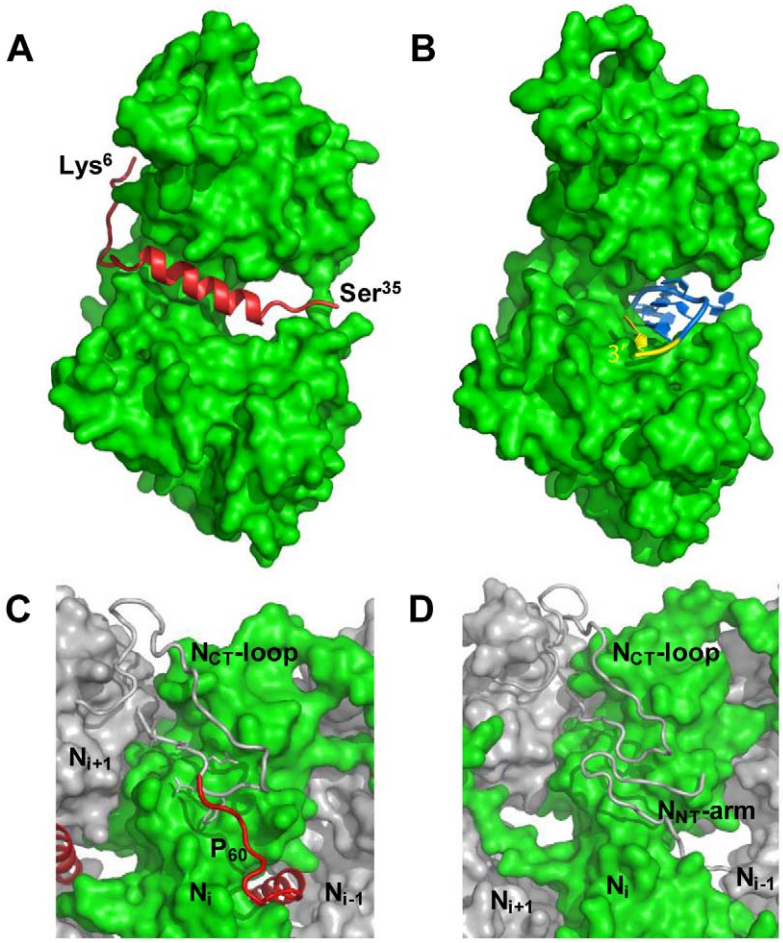

Figure 4. P binding hinders RNA binding and self-assembly of soluble N. (A) Representations of one protomer from the $N_{\Delta21}{}^0$-P_{60} complex. The N protomer is shown as space filling model in green and P_{60} is shown as a cartoon representation in red. The visible N- and C-terminal residues of P_{60} are labeled. (B) Representations of one protomer from the w.t. N-RNA complex. The 3′ terminal nucleotide of the RNA molecule is shown in yellow. These representations show that P_{60} fills the RNA-binding cavity on the side of N that accommodates the 3′-end of the RNA molecule. (C, D) Close-up of the interactions between exchangeable sub-domains in the circular $N_{\Delta21}{}^0$-P_{60} and N-RNA complexes. In the w.t. N-RNA complex (D), the N_{NT}-arm of protomer N_{i-1} contacts the N_{CT}-loop of protomer N_{i+1} while both sub-domains are docked on the back-side of protomer N_i (in green). In the $N_{\Delta21}{}^0$-P_{60} complex (C), the N-terminal extremity of P_{60} docks on protomer N_i (in green) at the position of the N_{NT}-arm of protomer N_{i-1} and contacts the N_{CT}-loop of protomer N_{i+1}. These representations suggest that P_{60} interferes with the assembly of N in the absence of RNA.
doi:10.1371/journal.ppat.1002248.g004

electrostatic surface potential of N, notably reducing the positive surface potential on one side of the molecule, and may thereby affect the side-by-side interaction with another N molecule.

From the results presented here, we propose a hypothesis for the encapsidation of a newly synthesized RNA molecule during viral genome replication. By forming a complex with P, a nascent N molecule is prevented from binding to host-cell RNA and is preserved in a soluble form. During RNA replication, N is transferred to a growing RNA molecule and P is released. Little is known about the mechanism of this reaction or about the role played by the polymerase complex in this process. Our results show that the N_{NT}-arm stabilizes the multimeric N-RNA complex and therefore suggest that the multimeric N-RNA complex is more stable than the N^0-P complex. The transfer of N from the N^0-P complex to the growing N-RNA complex could simply be driven by a higher stability of the N-RNA complex. Upon transfer of N onto the RNA and release of P, the backside groove of N of the last added N molecule is liberated and becomes available for accepting the N_{NT}-arm of the next incoming N molecule (Figure 7A). By blocking the backside groove of N, the N-terminal part of P ensures that N molecules do not assemble into empty N polymers but assemble only onto an RNA molecule. It is also noteworthy that, in VSV, a high affinity binding site for the L protein was localized in the second half of the N-terminal disordered region of P [7,28]. The dynamic nature of the N-terminal region of P and the proximity of the two binding sites may have significance for the mechanism of action of the transcription/replication machinery. The binding of N^0 to P may prevent the simultaneous binding of L, or conversely, the simultaneous binding of N^0 and L may modify the activity of the polymerase.

In addition to its role in RNA encapsidation, the binding of the N-terminal region of P to N may also provide a mechanism for the initiation of (+)RNA synthesis at the genome 3′ end and of (−)RNA synthesis at the antigenome 3′ end [29,30]. Encapsidated RNA genome and antigenome are completely covered with the nucleoprotein and are not accessible to the RNA polymerase. However, the first N molecule at the 3′ extremity of nucleocapsids exposes its binding site for the N-terminal MoRE of P (Figure 7B). By binding to this surface, P may destabilize the N-RNA complex sufficiently to displace several nucleotides from the first N protomer and allow the polymerase access to the RNA.

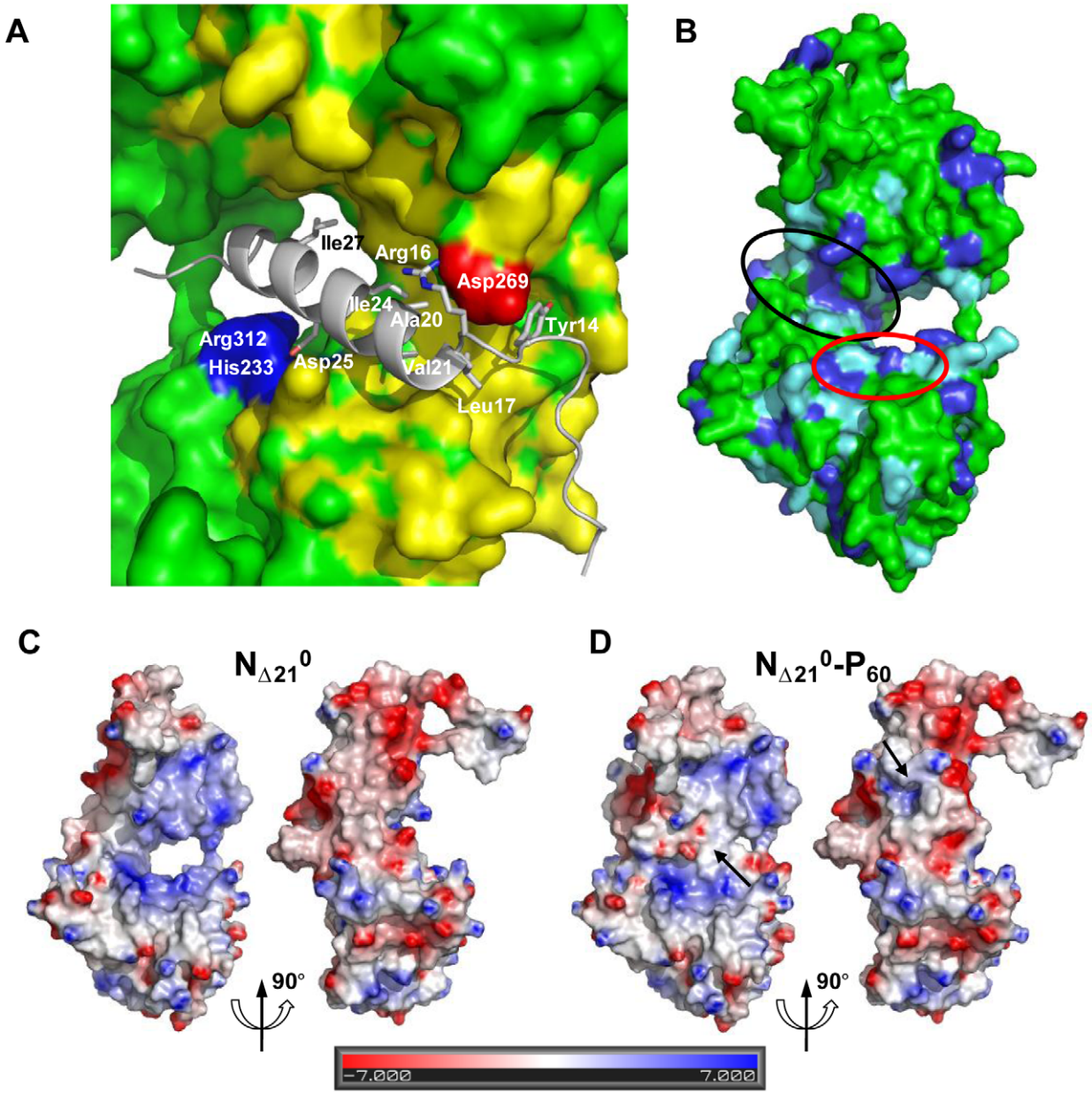

Figure 5. Surface properties and amino acid conservation in the P binding site. (A) Close up of the interface between RNA-free $N_{\Delta 21}$ and P_{60} showing the hydrophobic contacts and salt bridges. Residues 17 to 31 of P_{60} fold into an amphipathic α-helix that lies in a hydrophobic cavity formed by residues of the hinge region of N and is stabilized by hydrophobic contacts involving residues of P_{60} spaced i+3 or i+4 (Leu^{17}, Val^{21}, Ile^{24} and Ile^{27}). Tyr^{14} docks into a small cavity lined with hydrophobic residues. Hydrophobic side chains in N are colored in yellow and hydrophobic side chains of P_{60} are labeled. The complex is also stabilized by salt bridges between Asp^{25} of P_{60} and Arg^{312} and His^{233} of N (in blue) and between Arg^{16} of P_{60} and Asp^{269} of N (in red). (B) Amino acid sequence conservation between VSV and RAV N. Identical residues are shown in dark blue and similar residues are shown in light blue. The surface area circled in black shows the binding groove of P and the surface area circle in red shows the hydrophobic site common to both P and the bases at the 3′ end of the RNA. (C, D) Electrostatic surface potential of the $N_{\Delta 21}{}^0$ protein (C) compared with that of the $N_{\Delta 21}{}^0$-P_{60} complex (D). Both panels show in the same orientations the two sides of the $N_{\Delta 21}{}^0$ protein involved in binding the MoRE of P. The arrows indicate regions in which the electrostatic surface potential of N is modified by the presence of the peptide. The surface potentials were calculated with the Delphi program and are color-coded on the surface from red (negatively charged residues, −7 kcal/mol) to blue (positively charged residues, +7 kcal/mol).
doi:10.1371/journal.ppat.1002248.g005

Materials and Methods

Reconstitution of the $N_{\Delta 21}{}^0$-P and $N_{\Delta 21}{}^0$-P_{60} complexes

The cDNAs encoding vesicular stomatitis virus nucleoprotein or a fragment of this protein deleted of the 21 N-terminal residues were amplified by PCR and introduced into the pET-M40 plasmid (EMBL) using NcoI and XhoI restriction sites. The resulting constructs code for chimeric proteins that comprise an N-terminal maltose binding protein tag (MBP) and a tobacco etch virus (TEV) cleavage site. The cDNA encoding the 60 first N-terminal amino acids of VSV P (P_{60}) was amplified by PCR and cloned into the pET28a plasmid containing a C-terminal His_6-tag

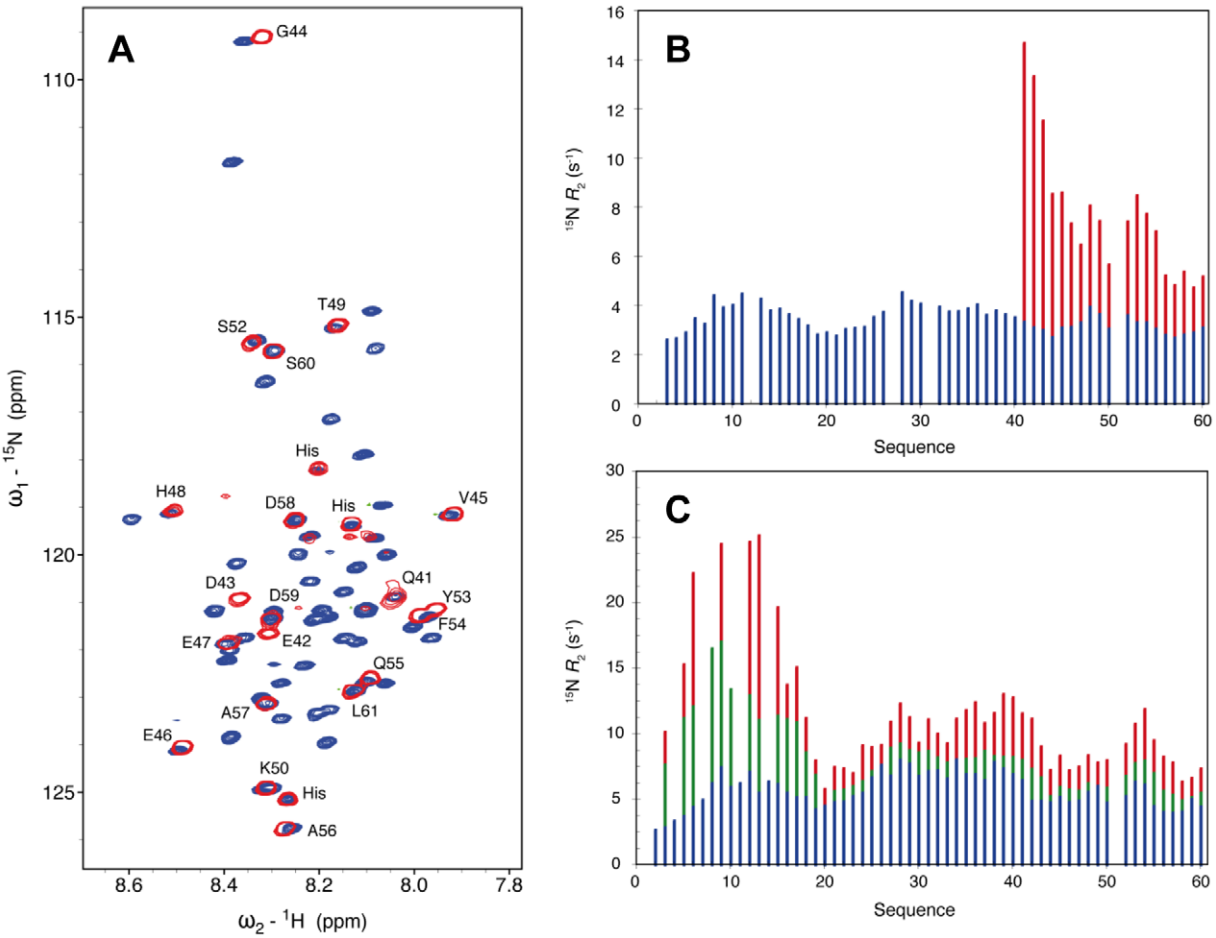

Figure 6. The N-terminal and C-terminal region of P_{60} flanking the MoRE exhibits conformational flexibility in the soluble complex. (A) Comparison of the 2D ^{1}H-^{15}N HSQC NMR spectra of free ^{15}N, ^{13}C, ^{2}H-labelled P_{60} (blue) and in complex with $N_{\Delta 21}$ (red). Both spectra were recorded at 14.1 T and 25°C in 20 mM Tris-HCl, 150 mM NaCl, 50 mM Glu, 50 mM Arg with 10% D_2O adjusted to pH 6.0. The labels indicate the assignment of the resonances of the complex. (B) ^{15}N R_2 spin relaxation rates measured under the same conditions as (A) for the free ^{15}N-labeled P_{60} (blue) and the $N_{\Delta 21}{}^0$-P_{60} complex (red). (C) ^{15}N R_2 spin relaxation rates measured at 14.1 T and 10°C of the free ^{15}N-labeled P_{60} (blue), a mixture of 0.27 mM ^{15}N-labeled P_{60} and 0.09 mM unlabeled MBP-$N_{\Delta 21}$ (green) and a mixture of 0.24 mM ^{15}N-labeled P_{60} and 0.17 mM unlabeled MBP-$N_{\Delta 21}$ (red).
doi:10.1371/journal.ppat.1002248.g006

and a linker of two amino-acids (EL) using NcoI and XhoI restriction sites. All constructions were checked by DNA sequencing.

The plasmids were transformed into *Escherichia coli* Rosetta (DE3) cells and the expression of the recombinant proteins was induced with 1 mM isopropyl-1-thio-β-d-galactopyranoside (IPTG) for 18 h at 16°C. Cells were harvested by centrifugation, suspended in buffer A (20 mM Tris–HCl, pH 7.5, 150 mM NaCl, 5 mM DTT) containing protease inhibitors (Complete EDTA-Free, Roche Diagnostics) and disrupted by sonication. The extract was centrifuged at 20,000 g during 30 min at 4°C and the supernatant was filtered (0.45 µm). The MBP-fusion proteins were purified by affinity chromatography on amylose resin (New England Biolabs) followed by size exclusion chromatography (SEC) on a Superdex S200 column (GE Healthcare) equilibrated in buffer A. P_{60} was purified by affinity chromatography on a Ni^{2+} resin column (Quiagen) followed by SEC on a Superdex S75 column (GE Healthcare) equilibrated in buffer A supplemented with 50 mM Glu and 50 mM Arg. Samples for NMR spectroscopy were produced in M9 minimal medium containing MEM vitamins (Gibco). For producing ^{15}N-labeled P_{60}, the medium was supplemented with 1.0 $g.L^{-1}$ of $^{15}NH_4Cl$ and 2.0 $g.L^{-1}$ of unlabeled glucose, while for producing ^{15}N, ^{13}C, ^{2}H-labeled P_{60} the minimal medium was prepared in D_2O and supplemented with 1.0 $g.L^{-1}$ of $^{15}NH_4Cl$ and 2.0 $g.L^{-1}$ of ^{13}C glucose.

The $N_{\Delta 21}{}^0$-P_{60} complex was prepared by incubating overnight at 4°C an excess of P_{60} with the MBP-$N_{\Delta 21}$-RNA complexes. The MBP-$N_{\Delta 21}{}^0$-P_{60} complex was purified by Ni^{2+} chelate affinity chromatography by using the His-tag present on P_{60} to remove the excess of free MBP-$N_{\Delta 21}$-RNA complex, followed by SEC on a Superdex S200 column equilibrated in buffer A and amylose affinity chromatography to eliminate unbound P_{60}.

The MBP tag was removed by incubating the protein with the TEV protease overnight at 4°C. The N protein contains the additional N-terminal tripeptide GAM. The $N_{\Delta 21}{}^0$-P_{60} complex was then purified using a Ni^{2+} chelate affinity chromatography followed by SEC on a Superdex S200 column equilibrated in buffer A. This procedure yielded pure $N_{\Delta 21}{}^0$-P_{60} complex. The samples were checked by SDS-PAGE using denaturing 4–20% gradient PAGE (Biorad).

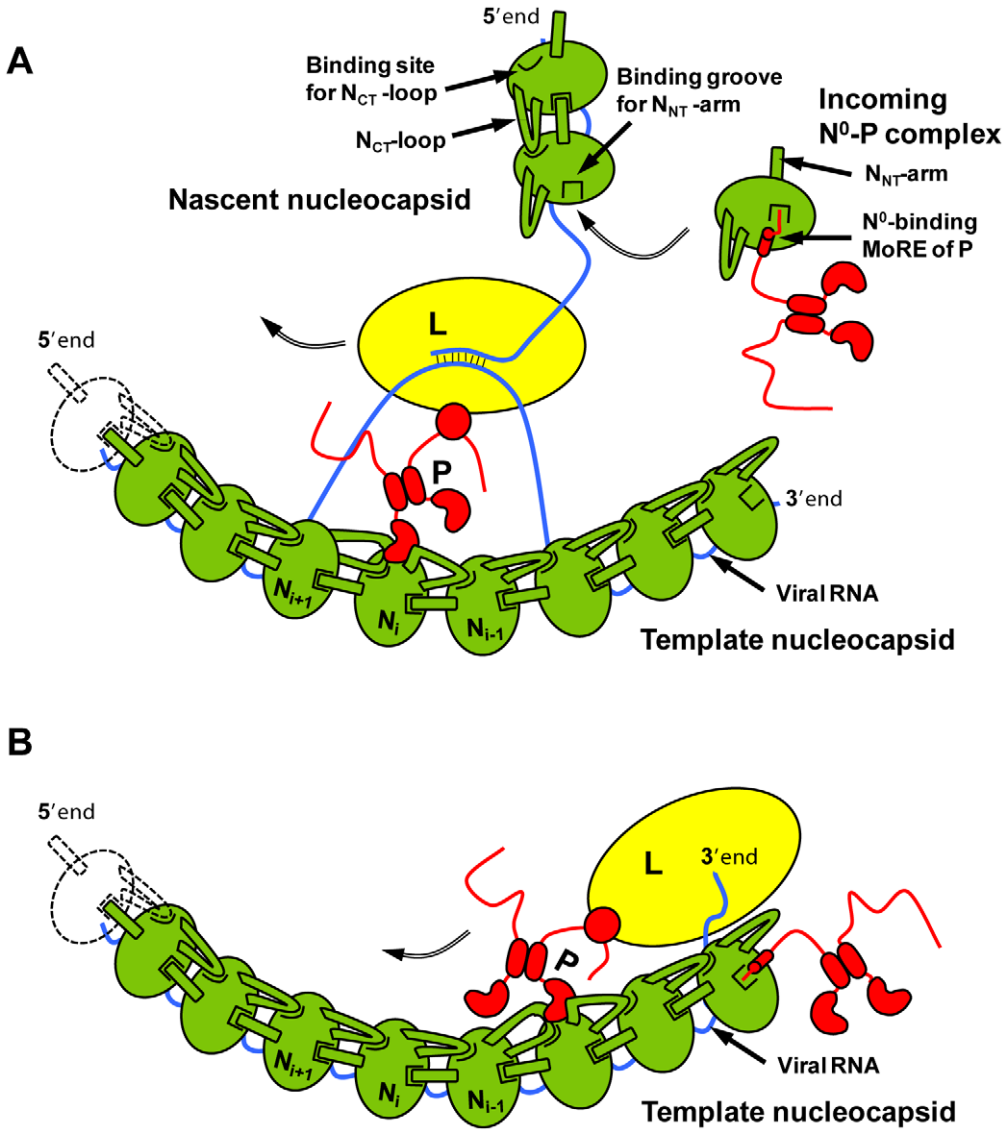

Figure 7. Schematic representations of the mechanism of RNA replication of VSV. The nucleoprotein (in green) forms with the RNA genome (blue line) the active template for the polymerase complex comprising the L (in yellow) and P (in red) proteins. (A) Encapsidation during RNA replication. During replication, the newly synthesized antigenomic or genomic RNA is encapsidated by nascent N molecules that are transferred from the soluble N^0-P complex. In the N^0-P complex, the N-terminal MoRE of P prevents host-cell RNA binding by obstructing the RNA binding groove and the self-assembly of N by interfering with the docking of the N_{NT}-arm of another N. Upon the transfer of N to the growing viral RNA P is released, the binding groove for the N_{NT}-arm is freed in the RNA-bound form and can accept the next incoming N molecule. (B) Initiation of RNA synthesis. By binding at the 3′ extremity of the nucleocapsid, the N-terminal MoRE of P might displace nucleotides from the N molecule and allow the polymerase to initiate RNA synthesis.
doi:10.1371/journal.ppat.1002248.g007

Size exclusion chromatography (SEC) combined with detection by multi-angle laser light scattering (MALLS) and refractometry: SEC-MALLS

SEC was performed with a Superdex S200 column (GE Healthcare) equilibrated in 20 mM Tris–HCl, pH 7.5, 150 mM NaCl. Separations were performed at 20°C with a flow rate of 0.5 $ml.min^{-1}$. 50 µL of a protein solution at a concentration ranging from 2.7 to 8.0 $mg.mL^{-1}$ were injected. On-line multi-angle laser light scattering (MALLS) detection was performed with a DAWN-EOS detector (Wyatt Technology Corp., Santa Barbara, CA) using a laser emitting at 690 nm. Protein concentration was measured on-line by refractive index measurements using a RI2000 detector (Schambeck SFD) and a refractive index increment $dn/dc = 0.185$ $mL.g^{-1}$. Data were analyzed and weight-averaged molecular masses (M_w) were calculated using the software ASTRA V (Wyatt Technology Corp., Santa Barbara, CA) as described previously [11]. For size determination, the column was calibrated with proteins of known Stokes' radius (R_S) [31].

Small angle X-ray scattering (SAXS) and *ab initio* modeling

SAXS data were collected at the European Synchrotron Radiation Facility (E.S.R.F., Grenoble, France) on beamline ID14-3. The sample-to-detector distance was 1 m and the wavelength of the X-rays was 0.931 Å. Samples were contained

in a 1.9 mm wide quartz capillary. The exposition time was optimized for reducing radiation damage. Data acquisition was performed at 20°C. Data reduction was performed using the established procedure available at ID14-3 and buffer background runs were subtracted from sample runs.

The SAXS profile of the $N_{\Delta 21}{}^0$-P_{60} complex was recorded for scattering vectors, $q = \frac{4\pi \sin\theta}{\lambda}$, in the range $0.05\ nm^{-1} < q < 3.5\ nm^{-1}$. The profiles obtained at three different protein concentrations 2.7–8.0 $mg.mL^{-1}$ had the same shape and were flat at low q values indicating the absence of significant aggregation (Figure S4A). The radius of gyration and forward intensity at zero angle (I(0)) were determined with the programs PRIMUS [32] by using the Guinier approximation at low q values (Figure S4B), in a $q \,.\, R_g$ range up to 1.3:

$$\ln I(q) = \ln I(0) - \frac{R_g^2 q^2}{3} \quad (1)$$

The forward scattering intensity was calibrated using bovine serum albumin and lysozyme as references. The radius of gyration, R_g, and the pair distance distribution function, P(r), were calculated with the program GNOM [33] (Figure S4C). The maximum dimension (D_{max}) value was adjusted so that the R_g value obtained from GNOM agreed with that obtained from the Guinier analysis. The R_g values showed no significant dependence on protein concentration, confirming the absence of aggregation or intermolecular interactions in the concentration range used in this study. The measured R_g value of 2.7 ± 0.1 nm (Table S1 in Text S1), and the molecular mass of 65 ± 15 kDa derived from the scattering intensity at zero angle, I_0, were in agreement with SEC-MALLS results. Additionally, the distance distribution function (Figure S4C) and the Kratky plot (Figure S4D) were typical of globular, folded proteins.

Ab initio low-resolution bead model reconstructions of the $N_{\Delta 21}{}^0$-P_{60} complex were performed from the scattering curves using the program DAMMIF [19]. This program restores a low-resolution shape of the protein as a volume filled with densely packed spheres (dummy atoms) that reproduces the experimental scattering curve by a simulated annealing minimization procedure. DAMMIF minimizes the interfacial area between the molecule and the solvent by imposing compactness and connectivity constraints. 20 independent models were generated with DAMMIF with no symmetry restriction and were combined with the program DAMAVER [34] yielding an average model that exhibited the common structural features of all reconstructions. The models were aligned pairwise by minimizing the normalized spatial discrepancy (NSD) score with the program SUPCOMB [35]. The mean NSD score of 0.75 (values ranging from 0.74 to 0.77) indicated an adequate convergence of the models [34]. All figures were generated with PyMOL (http://www.pymol.org).

Crystallization, data collection and structure determination and refinement

Crystallization conditions were screened by the hanging drop vapor diffusion method using a PixSys4200 Cartesian robot (high-throughput crystallization laboratory at EMBL Grenoble, France). The screen was performed by combining 0.1 µl of protein solution at 8 $mg.mL^{-1}$ in buffer A with 0.1 µl of Hampton Crystal Screen solutions. Hits were reproduced manually. The $N_{\Delta 21}{}^0$-P_{60} complex crystallized at 20°C in 0.1 M sodium acetate buffer, pH 4.6, containing 4% (w/v) of PEG4000. Single crystals were harvested from the drop, briefly soaked in the reservoir solution supplemented with 25% glycerol and flash frozen in liquid nitrogen at 100 K before data collection. X-ray diffraction data were collected at a wavelength of 0.933 Å on the ID14-2 beamline at the ESRF (Grenoble, France).

The data were processed using the program iMosflm [36] and scaled with the program Scala from the ccp4 suite [37]. The structure was solved by molecular replacement with the program Phaser [38] using residues 22 to 422 of a protomer of N (2GIC, chain E) extracted from the N-RNA crystal structure [15] as a search model. The visible part of P_{60} was assigned and constructed with the program Buccaneer [39], and the overall structure was refined to 3.0 Å resolution using Coot [40] and Refmac5 [41]. The quality of the model was checked with PROCHECK [42]. Data collection and refinement statistics are summarized in Table 1.

The $N_{\Delta 21}{}^0$-P_{60} complex was crystallized in space group $P2_12_12$. The crystallographic asymmetric unit contained five protomers of $N_{\Delta 21}{}^0$-P_{60} complex. Each protomer includes residues 22 to 422 of N and residues 6 to 33 of P_{60}. In some protomers, residues 34 and 35 could also be constructed.

NMR spectroscopy

NMR experiments were performed on a Varian spectrometer operating at a ^1H frequency of 600 MHz. All samples contained 20 mM Tris-HCl, 150 mM NaCl, 50 mM Glu, 50 mM Arg with 10% D_2O adjusted to pH 6.0. The concentration of free ^{15}N, ^{13}C, ^2H-labeled P_{60} was 0.9 mM and the concentration of the $N_{\Delta 21}{}^0$-P_{60} complex (^{15}N, ^{13}C, ^2H-labeled P_{1-60} in complex with unlabeled N) was 0.28 mM. In the titration experiment, ^{15}N-labeled P_{60} was initially at 0.28 mM. MBP- $N_{\Delta 21}$ was added at final concentrations of 0.09 mM or 0.17 mM. ^{15}N R_2 (CPMG) relaxation experiments were acquired using standard pulse sequences [43]. The spectra were acquired with a sweep width of 8.0 kHz and 512 complex points in the ^1H dimension, and a sweep width of 1.2 kHz and 200 complex points in the ^{15}N dimension. The magnetization decay was sampled at 10, 30, 50, 70, 90, 130, 170, 210 and 250 ms and the peak heights were used to extract the relaxation rates. To obtain estimates of the errors on the relaxation rates, a repeat measurement of one of the relaxation delays (70 ms) was carried out.

Supporting Information

Text S1 This file contains seven additional figures named S1 to S7 and an additional table S1.
(DOC)

Acknowledgments

We thank Ivan Ivanov and Danielle Blondel for helpful discussions. We thank the Partnership for Structural Biology for the excellent structural biology environment. Crystallographic coordinates and structure factors are deposited in the Protein Data Bank with accession code 3PMK.

Author Contributions

Conceived and designed the experiments: CL FY MRJ MB RWHR MJ. Performed the experiments: CL FY NT EAR MRJ MB. Analyzed the data: CL FY NT MRJ MB RWHR MJ. Contributed reagents/materials/analysis tools: CL FY EAR MRJ MB MJ. Wrote the paper: CL MRJ MB RWHR MJ.

References

1. Ge P, Tsao J, Schein S, Green TJ, Luo M, et al. (2010) Cryo-EM model of the bullet-shaped vesicular stomatitis virus. Science 327: 689–693.
2. Arnheiter H, Davis NL, Wertz G, Schubert M, Lazzarini RA (1985) Role of the nucleocapsid protein in regulating vesicular stomatitis virus RNA synthesis. Cell 41: 259–267.
3. Patton JT, Davis NL, Wertz GW (1984) N protein alone satisfies the requirement for protein synthesis during RNA replication of vesicular stomatitis virus. J Virol 49: 303–309.
4. Peluso RW, Moyer SA (1988) Viral proteins required for the in vitro replication of vesicular stomatitis virus defective interfering particle genome RNA. Virology 162: 369–376.
5. Howard M, Wertz G (1989) Vesicular stomatitis virus RNA replication: a role for the NS protein. J Gen Virol 70(Pt 10): 2683–2694.
6. Masters PS, Banerjee AK (1988) Complex formation with vesicular stomatitis virus phosphoprotein NS prevents binding of nucleocapsid protein N to nonspecific RNA. J Virol 62: 2658–2664.
7. Chen M, Ogino T, Banerjee AK (2007) Interaction of vesicular stomatitis virus P and N proteins: Identification of two overlapping domains at the N-terminus of P that are involved in N0-P complex formation and encapsidation of viral genome RNA. J Virol 81: 13478–13485.
8. Mavrakis M, Mehouas S, Real E, Iseni F, Blondel D, et al. (2006) Rabies virus chaperone: identification of the phosphoprotein peptide that keeps nucleoprotein soluble and free from non-specific RNA. Virology 349: 422–429.
9. Curran J, Marq JB, Kolakofsky D (1995) An N-terminal domain of the Sendai paramyxovirus P protein acts as a chaperone for the NP protein during the nascent chain assembly step of genome replication. J Virol 69: 849–855.
10. Zhang X, Green TJ, Tsao J, Qiu S, Luo M (2008) Role of intermolecular interactions of vesicular stomatitis virus nucleoprotein in RNA encapsidation. J Virol 82: 674–682.
11. Gérard FCA, Ribeiro E, Albertini A, Zaccai G, Ebel C, et al. (2007) Unphosphorylated Rhabdoviridae phosphoproteins form elongated dimers in solution. Biochemistry 46: 10328–10338.
12. Gérard FCA, Ribeiro EA, Leyrat C, Ivanov I, Blondel D, et al. (2009) Modular organization of rabies virus phosphoprotein. J Mol Biol 388: 978–996.
13. Leyrat C, Jensen MR, Ribeiro EA, Gérard F, Ruigrok R, et al. (2011) The N^0-binding region of the vesicular stomatitis virus phosphoprotein is globally disordered but contains transient α-helices. Prot Sci 20: 542–556.
14. Albertini AA, Wernimont AK, Muziol T, Ravelli RB, Clapier CR, et al. (2006) Crystal structure of the rabies virus nucleoprotein-RNA complex. Science 313: 360–363.
15. Green TJ, Zhang X, Wertz GW, Luo M (2006) Structure of the vesicular stomatitis virus nucleoprotein-RNA complex. Science 313: 357–360.
16. Ribeiro EA, Leyrat C, Gérard FC, Albertini AA, Falk C, et al. (2009) Binding of rabies virus polymerase cofactor to recombinant circular nucleoprotein-RNA complexes. J Mol Biol 394: 558–575.
17. Mavrakis M, Iseni F, Mazza C, Schoehn G, Ebel C, et al. (2003) Isolation and characterisation of the rabies virus N degrees-P complex produced in insect cells. Virology 305: 406–414.
18. Ding H, Green TJ, Lu S, Luo M (2006) Crystal structure of the oligomerization domain of the phosphoprotein of vesicular stomatitis virus. J Virol 80: 2808–2814.
19. Franke D, Svergun DI (2009) DAMMIF, a program for rapid ab-initio shape determination in small-angle scattering. J Appl Cryst 42: 342–346.
20. Luo M, Green TJ, Zhang X, Tsao J, Qiu S (2007) Conserved characteristics of the rhabdovirus nucleoprotein. Virus Res 129: 246–251.
21. Nayak D, Panda D, Das SC, Luo M, Pattnaik AK (2009) Single-amino-acid alterations in a highly conserved central region of vesicular stomatitis virus N protein differentially affect the viral nucleocapsid template functions. J Virol 83: 5525–5534.
22. Gupta AK, Banerjee AK (1997) Expression and purification of vesicular stomatitis virus N-P complex from Escherichia coli: role in genome RNA transcription and replication in vitro. J Virol 71: 4264–4271.
23. Castel G, Chteoui M, Caignard G, Prehaud C, Mehouas S, et al. (2009) Peptides that mimic the amino-terminal end of the rabies virus phosphoprotein have antiviral activity. J Virol 83: 10808–10820.
24. Ding H, Green TJ, Luo M (2004) Crystallization and preliminary X-ray analysis of a proteinase-K-resistant domain within the phosphoprotein of vesicular stomatitis virus (Indiana). Acta Crystallogr D Biol Crystallogr 60: 2087–2090.
25. Ribeiro EA, Jr., Favier A, Gerard FC, Leyrat C, Brutscher B, et al. (2008) Solution structure of the C-terminal nucleoprotein-RNA binding domain of the vesicular stomatitis virus phosphoprotein. J Mol Biol 382: 525–538.
26. Green TJ, Macpherson S, Qiu S, Lebowitz J, Wertz GW, et al. (2000) Study of the assembly of vesicular stomatitis virus N protein: role of the P protein. J Virol 74: 9515–9524.
27. Green TJ, Rowse M, Tsao J, Kang J, Ge P, et al. (2010) Access of RNA encapsidated in the nucleocapsid of vesicular stomatitis virus. J Virol 85: 2714–2722.
28. Emerson SU, Schubert M (1987) Location of the binding domains for the RNA polymerase L and the ribonucleocapsid template within different halves of the NS phosphoprotein of vesicular stomatitis virus. Proc Natl Acad Sci U S A 84: 5655–5659.
29. Abraham G, Banerjee AK (1976) Sequential transcription of the genes of vesicular stomatitis virus. Proc Natl Acad Sci U S A 73: 1504–1508.
30. Emerson SU (1982) Reconstitution studies detect a single polymerase entry site on the vesicular stomatitis virus genome. Cell 31: 635–642.
31. Uversky VN (1993) Use of fast protein size-exclusion liquid chromatography to study the unfolding of proteins which denature through the molten globule. Biochemistry 32: 13288–13298.
32. Konarev PV, Volkov VV, Sokolova A, M.H.J. K, Svergun DI (2003) PRIMUS: a Windows PC-based system for small-angle scattering data analysis. J Appl Cryst 36: 1277–1282.
33. Semenyuk AV, Svergun D (1991) GNOM - a program package for small-angle scattering data processing. J Appl Crystallog 24: 537–540.
34. Volkov VV, Svergun DI (2003) Uniqueness of ab initio shape determination in small-angle scattering. J Appl Cryst 36: 860–864.
35. Kozin MB, Svergun DI (2001) Automated matching of high- and low-resolution structural models. J Appl Cryst 34: 33–41.
36. Powell HR (1999) The Rossmann Fourier autoindexing algorithm in MOSFLM. Acta Crystallogr D Biol Crystallogr 55: 1690–1695.
37. Potterton E, Briggs P, Turkenburg M, Dodson E (2003) A graphical user interface to the CCP4 program suite. Acta Crystallogr D Biol Crystallogr 59: 1131–1137.
38. McCoy AJ, Grosse-Kunstleve RW, Adams PD, Winn MD, Storoni LC, et al. (2007) Phaser crystallographic software. J Appl Crystallogr 40: 658–674.
39. Cowtan KD (2006) The Buccaneer software for automated model building. Acta Crystallogr D Biol Crystallogr 62: 1002–1011.
40. Emsley P, Lohkamp B, Scott WG, Cowtan K (2010) Features and development of Coot. Acta Crystallogr D Biol Crystallogr 66: 486–501.
41. Murshudov GN, Vagin AA, Dodson EJ (1997) Refinement of macromolecular structures by the maximum-likelihood method. Acta Crystallogr D Biol Crystallogr 53: 240–255.
42. Laskowski RA, Macarthur MW, Moss DS, Thornton JM (1993) PROCHECK: a program to check the stereochemical quality of protein structures. J Appl Cryst 26: 283–291.
43. Farrow NA, Muhandiram R, Singer AU, Pascal SM, Kay CM, et al. (1994) Backbone dynamics of a free and phosphopeptide-complexed Src homology 2 domain studied by 15N NMR relaxation. Biochemistry 33: 5984–6003.